

Time-Lapse Seismic Imaging of Oceanic Fronts and Transient Lenses Within South Atlantic Ocean

Kathryn L. Gunn^{1,2} , Nicky White¹ , and Colm-cille P. Caulfield^{3,4} 

¹Bullard Laboratories, Department of Earth Sciences, University of Cambridge, Cambridge, UK, ²Rosenstiel School of Marine and Atmospheric Science, University of Miami, Miami, FL, USA, ³BP Institute, University of Cambridge, Cambridge, UK, ⁴Department of Applied Mathematics and Theoretical Physics, University of Cambridge, Cambridge, UK

Key Points:

- Time-lapse seismic imaging of deep oceanic front with spatial resolution of 5–10 m is presented
- Growth and decay of mesoscale tilted lens is visible at depth of 0.5–1 km over 9 days
- Rapid horizontal advection of thermohaline structures toward tilted lens is tracked

Supporting Information:

- Supporting Information S1
- Figure S1
- Figure S2
- Figure S3
- Figure S4

Correspondence to:

K. Gunn,
klg48@esc.cam.ac.uk;
kathy.gunn@rsmas.miami.edu

Citation:

Gunn, K. L., White, N., & Caulfield, C. P. (2020). Time-lapse seismic imaging of oceanic fronts and transient lenses within South Atlantic Ocean. *Journal of Geophysical Research: Oceans*, 125, e2020JC016293. <https://doi.org/10.1029/2020JC016293>

Received 2 APR 2020

Accepted 8 JUN 2020

Accepted article online 10 JUN 2020

Abstract Oceanic fronts play a pivotal role in controlling water mass transfer, although little is known about deep frontal structure on appropriate temporal and spatial scales. Here, we present a sequence of calibrated time-lapse images from a three-dimensional seismic survey that straddles the Brazil-Malvinas Confluence—a significant feature of the meridional overturning circulation. Eight vertical transects reveal the evolution of a major front. It is manifest as a discrete planar surface that dips at less than 2° and is traceable to 1.5–2 km depth. Its shape and surface expression are consistent with sloping isopycnal surfaces of the calculated potential density field and with coeval sea surface temperature measurements, respectively. Within the top ~1 km, where cold fresh water subducts beneath warm salty water, a series of tilted lenses are banked up against the sharply defined front. The largest of these structures is centered at 700 m depth and is cored by cold fresh water. Time-lapse imagery demonstrates that this tilted lens grows and decays over 9 days. It has a maximum diameter of $<34 \pm 0.13$ km and a maximum height of $<750 \pm 10$ m. Beneath 1 km, where horizontal density gradients are negligible, numerous deforming lenses and filaments on length scales of 10–100 km are being swept toward the advecting front.

Plain Language Summary Oceanic fronts (i.e., regions of rapid lateral changes in temperature and/or salinity) are key sites of water mass modification, primary productivity, and ocean-atmosphere exchange. However, fronts occupy a large range of scales (i.e., meters to kilometers and days to years) and present a significant observational challenge. Typically, measurements are restricted to small high-resolution surveys or to large surveys that have kilometer-scale gaps between sampling locations. We employ an acoustic imaging technique, which records energy reflected from temperature changes within the water column, to overcome these observational limitations. Vertical cross sections through the ocean are constructed over tens of kilometers that map temperature distribution on 10 m length scales. Critically, this analysis yields frontal observations that span a large range of spatial scales (i.e., 0.1–150 km) over a period of 1 week. This work presents novel time-lapse observations of frontal structure and behavior. Acoustic images reveal frontal dynamics that are occurring on larger, deeper, and faster scales than previously observed. Our analysis overcomes observational restrictions, revealing new frontal structure and behavior that have significant implications for future studies and ocean dynamics at fronts.

1. Introduction

Lateral and vertical gradients of physical properties at major oceanic fronts play a fundamental role in controlling the behavior of the global meridional overturning circulation (Cromwell & Reid, 1956). Convergence at these fronts gives rise to rapid, $O(100)$ m day^{−1}, vertical fluxes that provide pathways for transfer at the ocean-atmosphere boundary, within the surface mixed layer, and at abyssal depths (Pezzi et al., 2005; Spall, 1995; Thomas et al., 2008). As a result, enhanced vertical fluxes transport heat, salt, and nutrient-rich water into the euphotic zone that influence biologic productivity (Taylor & Ferrari, 2011; Tilstone et al., 2014). Oceanic fronts are associated with enhanced levels of turbulence and of energy dissipation (D'Asaro et al., 2011; Johnston et al., 2011; Nagai et al., 2012).

At fronts, gradients of physical properties are often observed within zones that can be hundreds of meters to tens of kilometers wide, persisting on time scales of days to years. Underway shipboard measurements have yielded high-resolution vertical profiles that are spaced at horizontal intervals of $O(10)$ km (e.g., Bianchi et al., 1993). In recent years, a range of towed and autonomous Lagrangian instruments has enabled

©2020. The Authors.

This is an open access article under the terms of the Creative Commons Attribution License, which permits use, distribution and reproduction in any medium, provided the original work is properly cited.

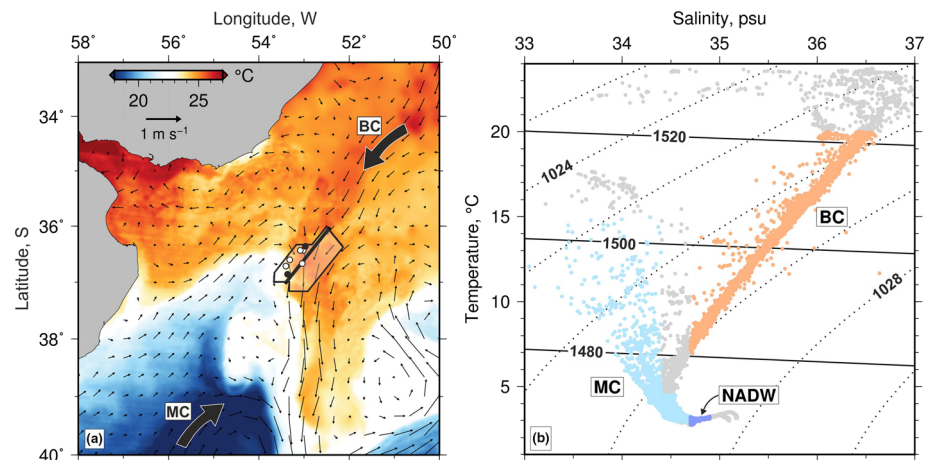


Figure 1. (a) Map of sea surface temperature for southwest Atlantic Ocean showing confluence of water masses. Red/blue colors = warm/cold water masses calculated for 13 February 2013 from Multi-scale Ultra-high Resolution Sea Surface Temperature (MUR-SST) satellite measurements (scale at top left-hand side); field of thin black arrows = average sea surface geostrophic current velocities calculated for 5 day composite centered on 15 February 2013 from Ocean Surface Current Analyses Real-time (OSCAR) satellite measurements (scale at top left-hand side); labeled arrows = Brazil Current (BC) and Malvinas (i.e., Falkland) Current (MC); transparent polygon = location of 3-D seismic reflection survey; thick black line within polygon = locus of eight transects displayed in Figure 3 and supporting information Figures S1 and S2 (see also Table 1); white circles = loci of seven near-coeval hydrographic casts (Table 2); pair of black circles = hydrographic casts used to calculate velocity profile shown in Figure 8h. (b) Temperature-salinity diagram based upon eight hydrographic casts located in panel a and interpreted in accordance with Piola and Matano (2017). Orange dots = principally Brazil Current but includes South Atlantic Central Water (SACW); pale blue dots = principally Malvinas Current but includes Antarctic Surface Water (AASW), Antarctic Intermediate Water (AAIW), and Upper Circumpolar Deep Water (UCDW); dark blue dots = North Atlantic Deep Water (NADW); gray dots = other water masses; labeled dotted/solid lines = contours of potential density/acoustic sound speed.

dense sampling of fronts (e.g., D'Asaro et al., 2011). This sampling usually extends over tens of square kilometers and depths of up to 400 m. Underwater gliders have significantly improved observations at fronts, providing dense measurements at meter-scale vertical and $O(1)$ km horizontal resolution (see review of Testor et al., 2019). Satellite measurements provide continuous surface observations that reveal the spatial and temporal evolution of fronts (e.g., Saraceno et al., 2004). Notwithstanding these developments, in situ volumetric studies of fronts continue to represent a significant challenge (Pallàs-Sanz et al., 2010). Computational constraints mean that the high-resolution grids required to characterize fronts are yet to be achieved, which means that fronts are usually omitted from quantitative models (Ferrari, 2011). In summary, observational and modeling challenges have tended to hamper our understanding of frontal dynamics and its role in oceanic and atmospheric circulation.

Seismic (i.e., acoustic) reflection surveying exploits low (e.g., 5–100 Hz) frequency sources and multiple towed cables with dense arrays of hydrophone receivers that enables oceanic fine structure to be imaged (Holbrook et al., 2003; Ruddick et al., 2009). Sound waves are transmitted through, and reflected from, temperature and, to a much lesser extent, salinity fluctuations on length scales that vary from tens of meters to tens of kilometers. Since acoustic reflections are principally generated by changes of temperature gradient that are typically $O(0.01)^{\circ}\text{C}$, the resultant seismic cross sections can be used to delineate and map ocean structure and water masses with contrasting thermohaline properties (Sallarès et al., 2009; Sheen et al., 2012). A typical cross section is >100 km long and >2 km deep. It can be acquired in a matter of hours and, critically, has approximately equal vertical and horizontal resolutions of $O(10)$ m.

Seismic surveying is a suitable tool for bridging the observational gap between fine-scale (i.e., 0.1–10 km) and large-scale (i.e., 10–1,000 km) structures. Significantly, the resultant stacked images can be inverted to obtain distributions of temperature and salinity (Dagnino et al., 2016; Gunn et al., 2018). In this way, physical properties of the water column at the time of imaging can be retrieved from legacy seismic reflection surveys, for which only limited coeval hydrographic measurements may exist. Here, we present time-lapse

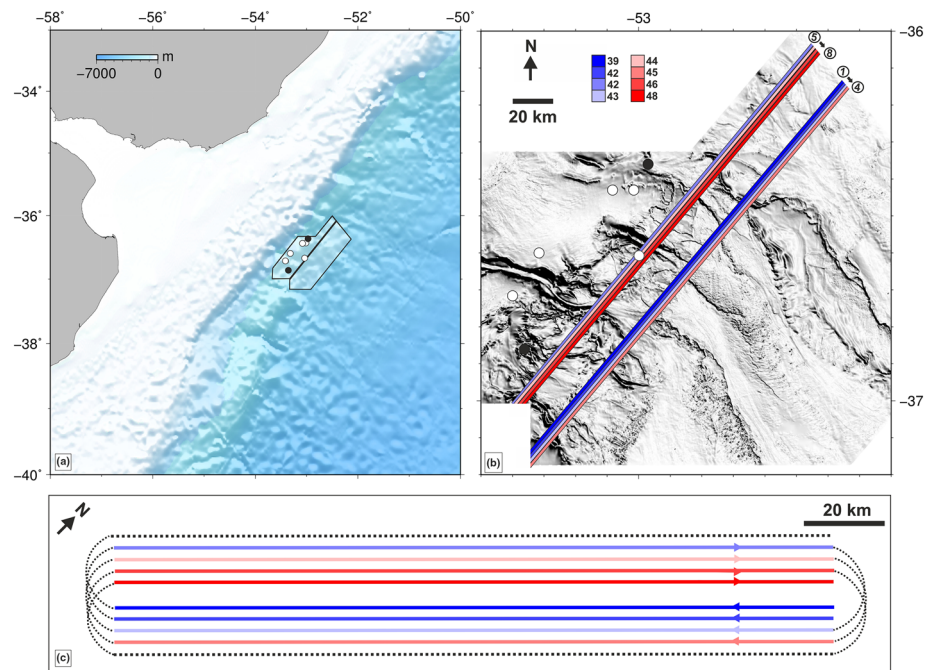


Figure 2. (a) Bathymetric map of southwest Atlantic Ocean. Transparent polygon = location of 3-D seismic reflection survey; thick black line within polygon = locus of eight transects described in text and displayed in Figures S1 and S2 (see also Table 1); white circles = loci of seven near-coeval hydrographic casts (Table 2); pair of black circles = hydrographic casts used to calculate geostrophic velocity profile shown in Figure 8g. (b) Detailed portion of bathymetric map shown in (a). Thick colored lines = seismic reflection Lines 1–8 colored by Julian day of acquisition; numbered white circles = acquired lines; white/black circles = near-coeval hydrographic casts as in (a). (c) Diagrammatic map showing configuration of racetrack acquisition for Sections 1–8 of 3-D seismic reflection survey. Black dashed lines = vessel tracks; thick colored lines = seismic reflection lines colored by Julian day of acquisition; thick black line = 20 km scale.

imagery extracted from a three-dimensional (3-D) seismic reflection survey that was acquired across the Brazil-Malvinas confluence of the southwest Atlantic Ocean (Figures 1 and 2). Our principal aim is to show how what is effectively volumetric imagery has the potential to identify and to analyze transient frontal structures at an oceanographically significant confluence on an unprecedented range of scales and depths. Note that coincident and dense hydrographic measurements, which would help to constrain the detailed fluid dynamical nature of these structures, were unavailable. Nevertheless, our observations have helped to identify features that have not previously been imaged in other ways. The quantitative nature of this imagery, together with corresponding distributions of physical properties, permit potential dynamical mechanisms to be identified. We hope that our results will motivate combined acquisition programs of hydrographic and seismic reflection surveys in jointly designed experiments.

2. Seismic Acquisition and Processing

Vertical images are extracted from a 3-D survey, which was acquired between November 2012 and April 2013 by Polarcus Limited OSE using Seismic Research Vessel *Amani*. This survey is owned by Administración Nacional de Combustibles, Alcoholes y Portland (ANCAP) and by Royal Dutch Shell. The acoustic source comprises a pair of airgun arrays, each of which has 36 guns with a combined volume of 70 L (i.e., 4,240 inch³). These airguns are primed with an air pressure of 14 MPa (i.e., 2,000 psi) and simultaneously fired every 10 s (i.e., every ~25 m along the ground). The combined bandwidth of the acoustic source is 5–100 Hz. Reflected waves are recorded along 10 streamers (i.e., acoustically sensitive cables), each of which is 6 km long, separated by 125 m, and towed at a depth of 9 m. Each streamer has 480 groups of hydrophones located at intervals of 12.5 m. The record sampling interval is 2 ms. Each pass of the vessel acquired a swath of data that is ~600 m wide and ~140–150 km long. The seismic images presented here are extracted

Table 1
Seismic Acquisition Information (See Also Figures 1a and 2)

Label	Length (km)	dd/mm/yyyy	Julian day	Azimuth
1	148	08/02/2013	39	NE-SW
2	149	11/02/2013	42	NE-SW
3	150	12/02/2013	43	NE-SW
4	150	14/02/2013	45	NE-SW
5	142	11/02/2013	42	SW-NE
6	142	13/02/2013	44	SW-NE
7	141	15/02/2013	46	SW-NE
8	140	17/02/2013	47	SW-NE

from the center of each swath. The vessel steamed with an average azimuth of 41° in what is known as a racetrack pattern at a speed of 2.5 m s^{-1} (Figure 2c).

The geometry of sources and receivers means that each position along a given traverse is sampled 120 times. This redundancy enables the signal-to-noise ratio to be increased by stacking seismic reflections from different shotpoint-receiver pairs that sample an identical position or common midpoint (CMP) along each traverse. Optimal stacking relies on careful estimates of root-mean-square acoustic sound speed, v_{rms} , as a function of depth in order to correct for the travel time delay for different raypaths within a single CMP gather. Individual functions of v_{rms} are manually

picked every 1.25 km. Other signal processing techniques include application of a 20–90 Hz band-pass filter with a roll-off of 24 dB per octave, muting of the bright seabed reflection, and removal of high amplitude acoustic energy that travels horizontally along the length of each streamer. Finally, seismic images were converted to depth using an average sound speed of $1,530 \text{ m s}^{-1}$. Spatial migration of these images is usually not required since the water column is characterized by slow and gradually varying sound speed.

Processed images represent vertical full-depth cross sections or slices through the oceanic volume. The vertical resolution of each image is given by $v/4f$ where v and f are the sound speed of the water column and the dominant frequency of the acoustic source, respectively. In this region, $v = 1,510 \pm 30 \text{ m s}^{-1}$ throughout the water column and $f = 35 \pm 5 \text{ Hz}$, which means that the vertical resolution is between 10 and 20 m. On seismic images that have been spatially migrated (or that do not require migration), horizontal resolution is equal to vertical resolution (i.e., it is not given by the radius of the first Fresnel zone; Yilmaz, 2001). Observed reflectivity is generated by changes in acoustic impedance, which is defined as the product of sound speed and density. Within the water column, acoustic impedance is predominantly controlled by sound speed variation, which depends upon temperature and, to a much lesser extent, salinity gradients. Thus, the reflectivity field contains useful information about temperature and salinity that is recoverable from detailed measurements of sound speed, v .

3. Deep Structure of Oceanic Front

3.1. Reflectivity Patterns

Confluent flow of warm salty Brazil Current (BC) and cold fresh Malvinas (i.e., Falkland) Current (MC) concentrates large-scale temperature and salinity gradients over a substantial region (Figure 1a; Gordon, 1989; Peterson & Stramma, 1991). At depths of up to several hundred meters, these subtropical and sub-Antarctic water masses have sharply contrasting properties. Although these water masses are distinct, the opposing effects of temperature and salinity gradients can act to produce density compensation (Figure 1b). Eight seismic transects, acquired across the northern portion of this confluence zone between 8 and 17 February 2013, are presented, interpreted, and analyzed (Figures S1 and S2 in the supporting information and Table 1). These transects provide time-lapse images of spatial and temporal variability of the Brazil-Malvinas Confluence, which have common features that can be described using one representative example (Figure 3).

A continuous and bright reflection that dips northward at $<2^\circ$ can be traced down to a depth of $1.7 \pm 0.05 \text{ km}$ (Figure 3b). At $\sim 300 \text{ m}$ depth, this dipping reflection splits into four discrete bright strands that wrap around acoustically transparent patches and define a series of tilted lenses, which outcrop at a range of 50–60 km and coincide with a marked change in sea surface temperature visible on satellite imagery (Figures 4 and 5). Similar splitting into discrete strands is observed beneath $\sim 500 \text{ m}$ at ranges of 85–100 km. This multi-stranded reflection represents the acoustic expression of a discrete front that is traceable from the sea surface to abyssal depths on all eight transects (supporting information). Northeast of the surface outcrop of the front, the seismic image is characterized by smooth, flat and horizontally discontinuous reflections. They constitute a thick, deep wedge of BC water that is banked against the front.

Southwest of the front, MC water is characterized by a complex swirling pattern of reflectivity that is visible down to the seabed. At ranges of 60–100 km, concentric reflections wrap around and define a prominent but

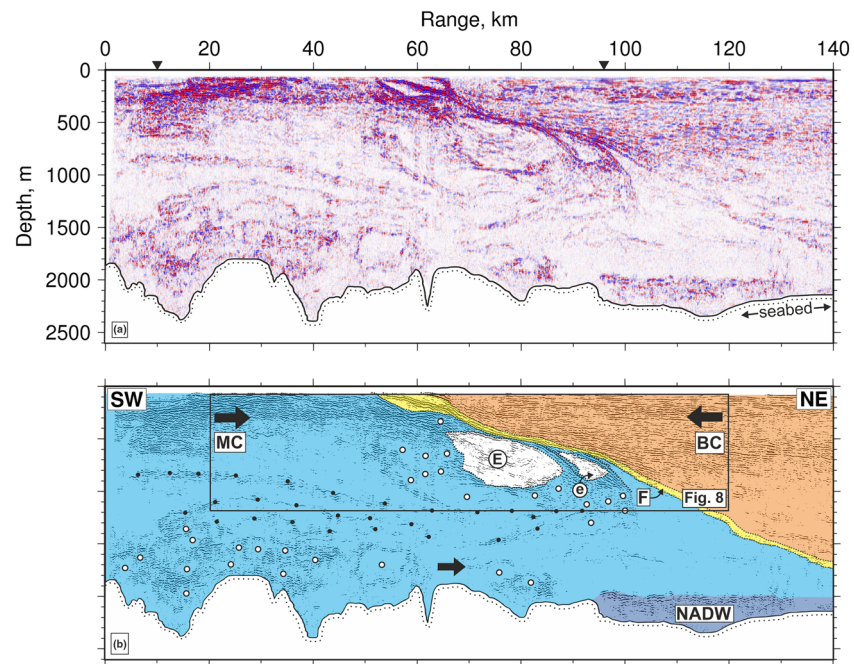


Figure 3. (a) Representative seismic section that crosses major oceanic front (Figure S2a). Red/blue stripes = positive/negative reflections that are generated by temperature changes as small as $\sim 0.01^{\circ}\text{C}$ within water column. Black triangles = loci of velocity analyses (Figure 4). (b) Generalized interpretation that emphasizes principal features. Orange shading = Brazil Current (BC); blue shading = Malvinas Current (MC); dark blue shading = putative dense layer of North Atlantic Deep Water (NADW); black arrows = large-scale flow; yellow dipping zone labeled F = discrete oceanic front dipping at $<2^{\circ}$ down to depth of $>1,600$ m; tilted white blobs labeled E and e = lens-shaped features of $O(10)$ km defined by reflections; white circles = centers of acoustically blank features of $O(1-10)$ km; black circles = tracking of elongated reflections; black box = portion of section from Figure 8.

acoustically transparent lens that has a diameter of 21 km and a thickness of 400 m (labeled 'E' on Figure 3b). The center of this tilted lens sits at a depth of 750 m and its upper surface abuts the front, which it appears to have deformed. A much smaller tilted lens is juxtaposed against its northeastern edge at a range of 92 km. A similar pair of lenses is visible on other transects, although their sizes vary from transect to transect. For example, the diameter of the bigger lens varies between 11 and 34 km, and its height varies between 250 and 750 m. Its inverse aspect ratio (i.e., height/width) is ~ 0.02 , which is consistent with f/N scaling, where $N = 3 \times 10^{-3} \text{ s}^{-1}$ and $f = 9 \times 10^{-5} \text{ s}^{-1}$ are the local buoyancy frequency and the Coriolis parameter, respectively (Table 3). Note that a spatially averaged value of N is estimated from the distributions of temperature and salinity shown in Figure 8. The perimeters of these lenses are characterized by sinusoidally shaped reflections that are interpreted as, and have the spectral characteristics of, internal waves (e.g., Sheen et al., 2009). Beneath ~ 500 m depth, MC water is characterized by numerous acoustically transparent and irregularly shaped lenses with diameters of 1–10 km (Figure 3b). At depths of 800 and 1,500 m, several elongated filament-like reflections can be traced horizontally from the southwestern edge of the profile toward the base of the biggest tilted lens.

3.2. Physical Properties

Distributions of temperature and salinity along this transect are calculated using an adapted iterative procedure (Gunn et al., 2018; Papenberg et al., 2010). Typical acoustic inverse approaches cannot easily be exploited since closely spaced coincident hydrographic observations of temperature and salinity are required to provide a long-wavelength background profile on length scales that are greater than 150 m. To sidestep this limitation, we construct the long-wavelength sound speed pattern by analyzing prestack seismic records (Figure 6). This pragmatic approach obviates the need for coincident and densely sampled hydrographic measurements and so it can be applied to legacy archives of uncalibrated seismic surveys. The long-wavelength variation of sound speed is calculated from a suite of individual functions of v_{rms} that are

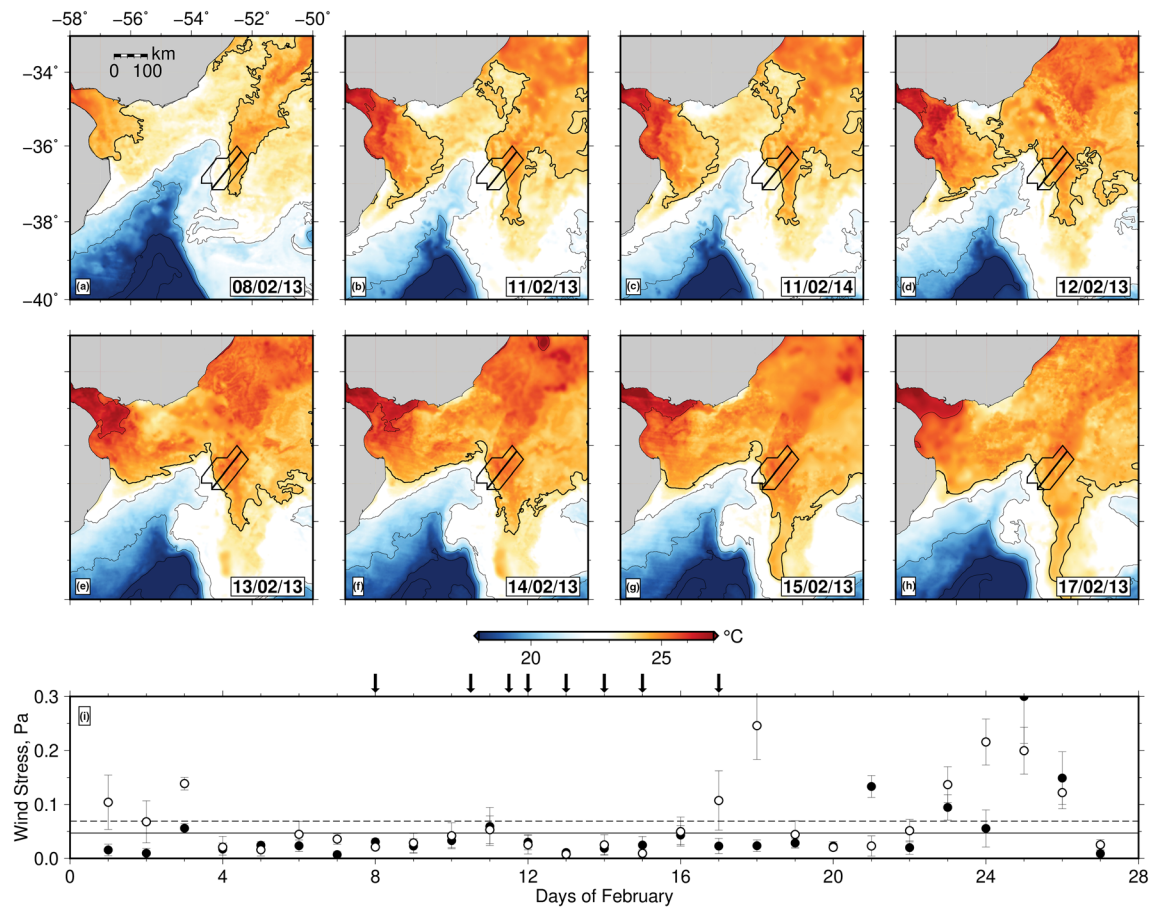


Figure 4. (a) Map of sea surface temperature for southwest Atlantic Ocean showing confluence of water masses on day that Section 1 was acquired (date listed at bottom right-hand side). Red/blue colors = warm/cold water masses calculated for 8 February 2013 from MUR-SST satellite measurements. Black polygon = location of 3-D seismic reflection survey; thick black line within polygon = locus of Sections 1–8 described in text; thin black lines = sea surface temperature contoured every 2°C; thick black line = 24°C contour. (b–h) Same for days that correspond to acquisition of Sections 2, 5, 3, 6, 4, 7, and 8, respectively (see Figure 2). Note date at lower right-hand corner. (i) Average wind stress as a function of day for region shown in other panels. Black/white circles = zonal/meridional values of wind stress; solid/dashed black line = monthly average for February 2013 of zonal/meridional wind stress; black arrows = acquisition times of seismic sections shown in panels a–h. Wind measurements are from Metop-A ASCAT satellite (Verspeek et al., 2010).

located every 1.25 km along the transect (Figures 6 and 7a). Vertical and horizontal moving averages are used to smooth the spatial variation of v_{rms} , which is then converted into interval sound speed, v_{int} , using the standard relationship (Figure 7b; Dix, 1955). The short wavelength variation of sound speed is separately extracted from the reflectivity field by exploiting

$$R = \frac{v_2 \rho_2 - v_1 \rho_1}{v_2 \rho_2 + v_1 \rho_1}, \quad (1)$$

where R is the reflection coefficient, v_1 and ρ_1 are the sound speed and density above a given reflective interface, and v_2 and ρ_2 are the sound speed and density beneath this interface (Yilmaz, 2001). The value of R is principally controlled by changes in v_1 and v_2 , and it is reasonable to assume that density varies as a function of depth in accordance with regional hydrographic measurements. The reconstructed long and short wavelength sound speed fields are merged and converted into temperature and salinity using a local temperature-salinity relationship and the equation of state for seawater (for more details see Gunn et al., 2018; Papenberg et al., 2010).

Our results demonstrate that the northeastern end of the transect is characterized by a layer of warm salty water (>10°C and >35 psu; Figures 8a and 8c). This layer thickens northeastward, coinciding with the

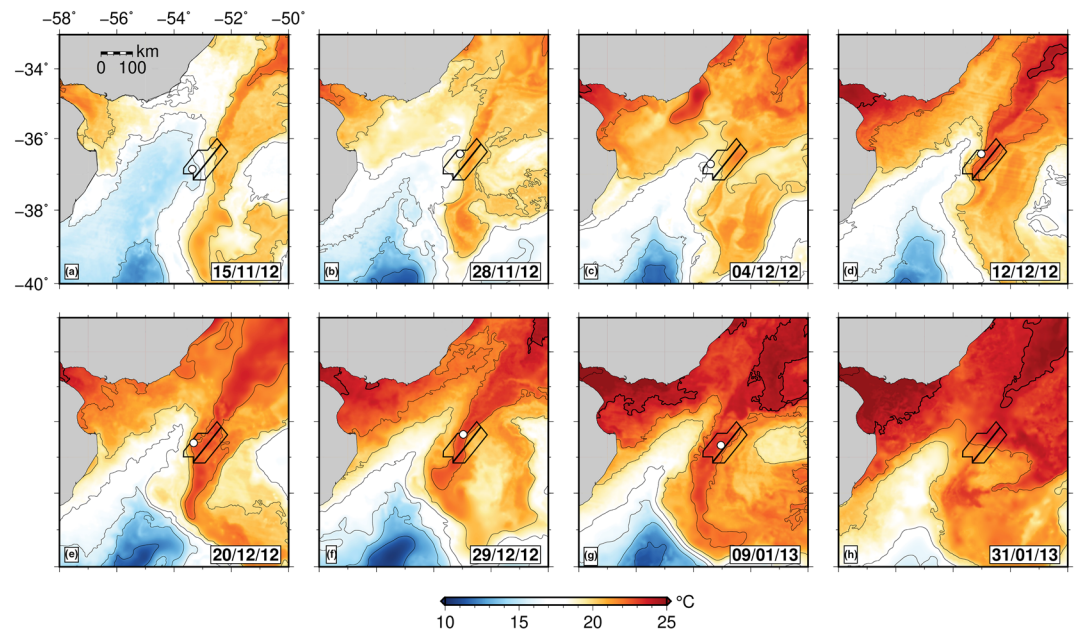


Figure 5. (a) Map of sea surface temperature for southwest Atlantic Ocean showing confluence of water masses on day that hydrographic probe T1 was acquired. Red/blue colors = warm/cold water masses calculated for 15 November 2012 from MUR-SST satellite measurements. Black polygon = location of 3-D seismic reflection survey; white circle = location of T1 hydrographic probe; thin black lines = sea surface temperature contoured every 2°C; thick black line = 24°C contour. (b–h) Same for days that correspond to acquisition of hydrographic probes T2–7 (see Figure 1a for scale). Note date at lower right-hand corner.

wedge of reflectivity that abuts the dipping front. Along the southwestern edge of the front, the water mass is cooler (i.e., $\leq 10^\circ\text{C}$) and fresher (i.e., ≤ 35 psu). This dramatic change of physical properties is consistent with measurements from near-coeval hydrographic casts as well as with satellite observations, which supports our interpretation that the northeastward band of dipping reflections represents a deeply penetrating front, separating distinct BC and MC water masses (Figures 8b and 8d). We note that water on the southwestern side of the front is not quite as cold and fresh as hydrographic measurements of MC indicate. Instead, it represents an intermediate water mass generated by mixing of subtropical and sub-Antarctic waters in the vicinity of the frontal zone (i.e., modified MC; Figure 1). Temperature and salinity values of $< 5^\circ\text{C}$ and > 34.4 psu at depths $\geq 1,000$ m are diagnostic of AAIW, CDW, and NADW waters (Figure 1b). The large tilted lens consists of a patch of cool ($3.3 \pm 1^\circ\text{C}$) and fresh (34.3 ± 0.5 psu) water, implying that it is sourced from the southwestern side of the front (i.e., modified MC water; Figures 8b and 8d).

Without dense and coeval hydrographic observations, it is challenging to use the adapted iterative procedure to resolve shorter (≤ 100 m) wavelength variations of temperature and salinity (Gunn et al., 2018). Nevertheless, we can directly compare our horizontally averaged profiles of temperature and salinity with near-coeval hydrographic measurements (Table 2). Although average values can be offset by up to 1°C and 0.5 psu, the adapted iterative procedure yields results that successfully reproduce the long-wavelength patterns on either side of the front (Figures 8b and 8d). It is likely that these offsets are the consequence of temporal differences of up to 4 months between acquisition of hydrographic and seismic surveys (Figures 4 and 5; Table 2). Thermoclinic and haloclinic thicknesses are coherent with measured BC and MC values, which are also consistent with weakening of reflectivity at depths of ~ 600 and $\sim 1,000$ m on each side of the front (Piola & Matano, 2017). We use these calculated distributions of temperature and salinity to constrain potential density, ρ_θ , and geostrophic current, u (i.e., Figures 8e and 8g). Our values are broadly consistent with estimates based upon near-coeval hydrographic measurements (Figures 8f and 8h).

Calculated isopycnal surfaces are consistent with a gently sloping (i.e., 3.5×10^{-2}) front (Figure 8e). The geostrophic stream function, ψ , which can show a better alignment with dipping seismic reflections, has also been

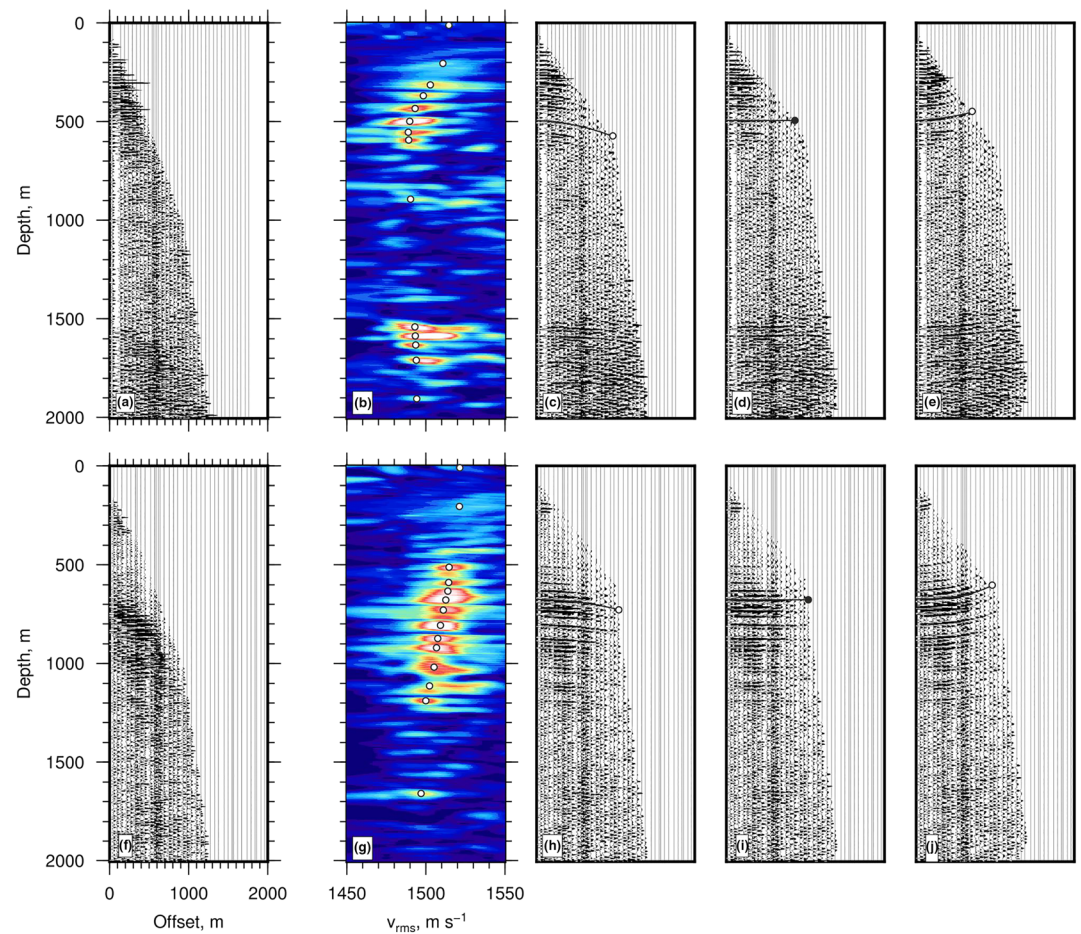


Figure 6. Sound speed analysis of CMP gathers from Section 5. (a) Uncorrected CMP gather at range of 10 km plotted as a function of offset distance between source and receiver and depth. (b) Contoured values of semblance as a function of offset distance and depth that show root-mean-square sound speed, v_{rms} . Warm colors = optimal values of v_{rms} that yield correct time delays; white circles = chosen v_{rms} picks. (c) Undercorrected CMP gather where selected v_{rms} values are too slow (i.e., $1,450 \text{ m s}^{-1}$). Line with open circle = undercorrected reflection. (d) Optimally corrected CMP gather using v_{rms} picks shown in panel b. Lines with solid circle = optimally corrected reflection. (e) Overcorrected CMP gather where selected v_{rms} values are too fast (i.e., $1,550 \text{ m s}^{-1}$). Line with open circle = overcorrected reflection. (f)–(j) Equivalent panels for CMP gather at range of 96 km.

determined (e.g., Meunier et al., 2015). Figure 8g indicates that ψ surfaces slope gently toward the northeast within the upper 700 m of the water column. We conclude that both ρ_θ and ψ fields are consistent with the geometry of reflectivity on length scales $>10 \text{ km}$. Below $\sim 700 \text{ m}$, contours of ρ_θ have negligible slope, which is consistent with the known density compensation of BC and MC at these depths (Figure 1b; Piola & Matano, 2017). Horizontal density gradients intensify close to the surface and create geostrophic shear along the frontal axis, which in turn produces a jet that is orientated along this axis. In Figure 8e, isopycnal surfaces slope toward the northeast, which implies flow to the southeast. This qualitative inference is corroborated by our estimate of u which is consistent with a southeastward directed jet with a velocity of $\sim 0.6 \text{ m s}^{-1}$ that is focused within the upper 500 m at a range of 50–60 km where a significant horizontal gradient occurs (Figure 8g). Significantly, this location coincides with four discrete reflective strands that delineate small tilted lenses within the front.

Relative vorticity close to the front, ζ , can be inferred from u , where $\zeta = \partial v / \partial x - \partial u / \partial y$. Along this segment of the Brazil-Malvinas Confluence, it is reasonable to assume that the value of ζ is dominated by contributions from the cross-front gradient, which means that the component in the y -direction can be neglected (e.g., Pollard & Regier, 1992). The calculated pattern of ζ shows that large-scale vorticity occurs at the

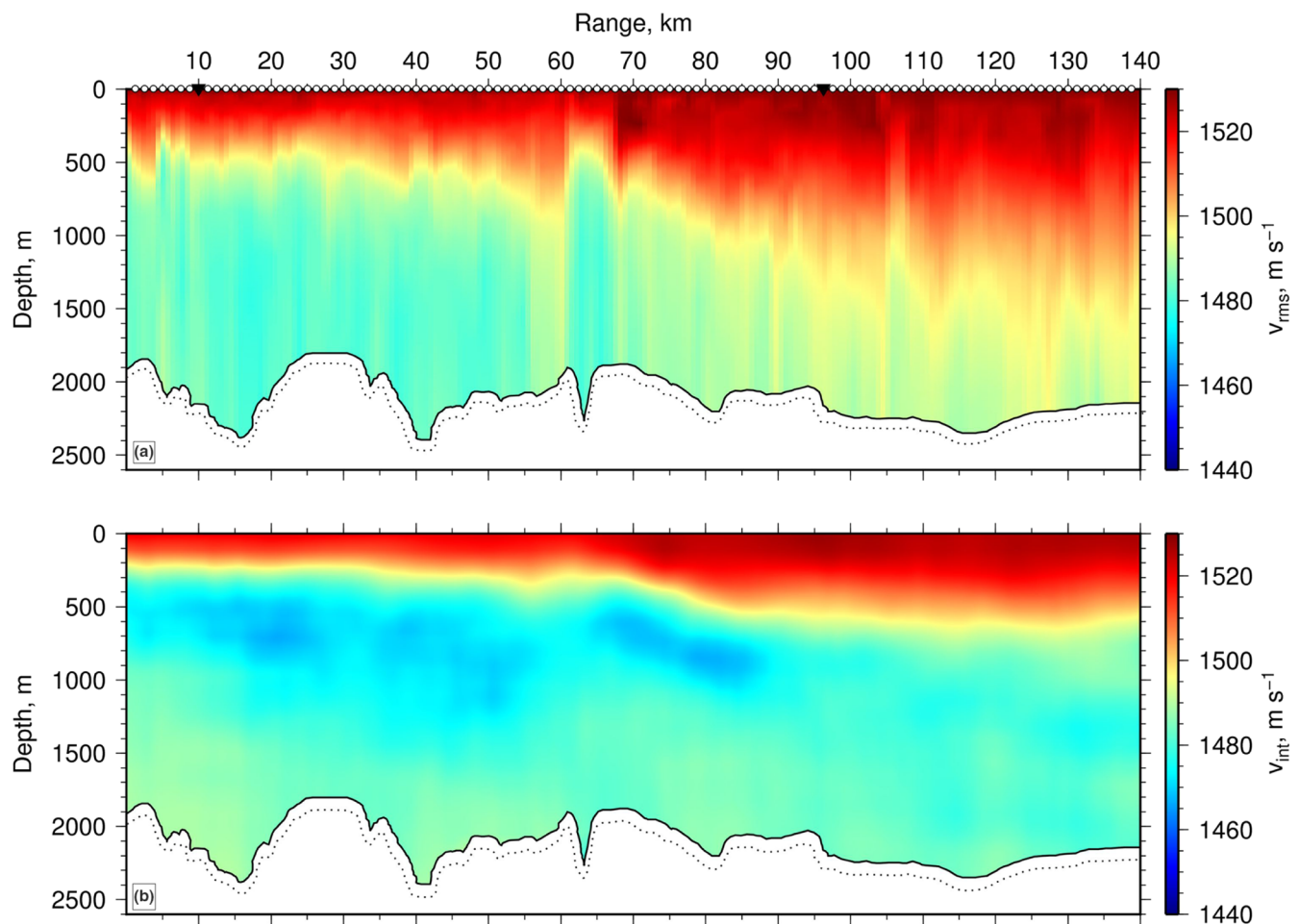


Figure 7. (a) Root-mean-square sound speed, v_{rms} , as a function of range for Section 5 (Figure S2a). White circles = loci of sound speed profiles that were picked every 1.25 km; black triangles = loci of CMP gathers displayed in Figure 6. (b) Interval sound speed, v_{int} , as a function of range calculated from v_{rms} using Dix equation (i.e., long-wavelength component of sound speed). Sound speed is vertically and horizontally smoothed using sliding windows of ~ 250 m and 12.5 km, respectively.

front. At depths shallower than 1 km, positive values of ζ indicate the cyclonic side that is located southwest of the front (Figure 8g). The large tilted lens has no resolvable vorticity.

4. Temporal Evolution of Frontal Structures

4.1. The Front

The front itself is imaged across the volume of the seismic survey and it is clearly visible on the eight representative transects presented in the supporting information. During survey acquisition, the vessel travels in a clockwise direction, crisscrossing the front in a series of shifting loops each of which incrementally translates by ~ 1 km toward the northeast. This so-called racetrack mode is adopted for operational reasons and, as a consequence, adjacent sail lines are acquired by a combination of broad turning and interleaving at different times (Figures 2b and 2c; Yilmaz, 2001). Thus, Sections 1–4 are acquired in the same compass direction such that they are colocated in space but not in time. Sections 5–8 are similarly arranged (see Table 1 for further details of acquisition). Since the front is oriented at a high angle to the sail direction, it is straightforward to determine frontal migration (Figure 4). During February 2013, the front advected southwestward at a rate of 15 ± 1 km day $^{-1}$. Coeval satellite measurements of sea surface temperature corroborate this value. For example, southwestward translation of the 24°C sea surface temperature contour yields an independent estimate of 14 ± 1 km day $^{-1}$ in agreement with other satellite observations, which indicate oscillation of the Brazil-Malvinas Confluence at this time of year (Garzoli & Garraffo, 1989; Saraceno et al., 2004).

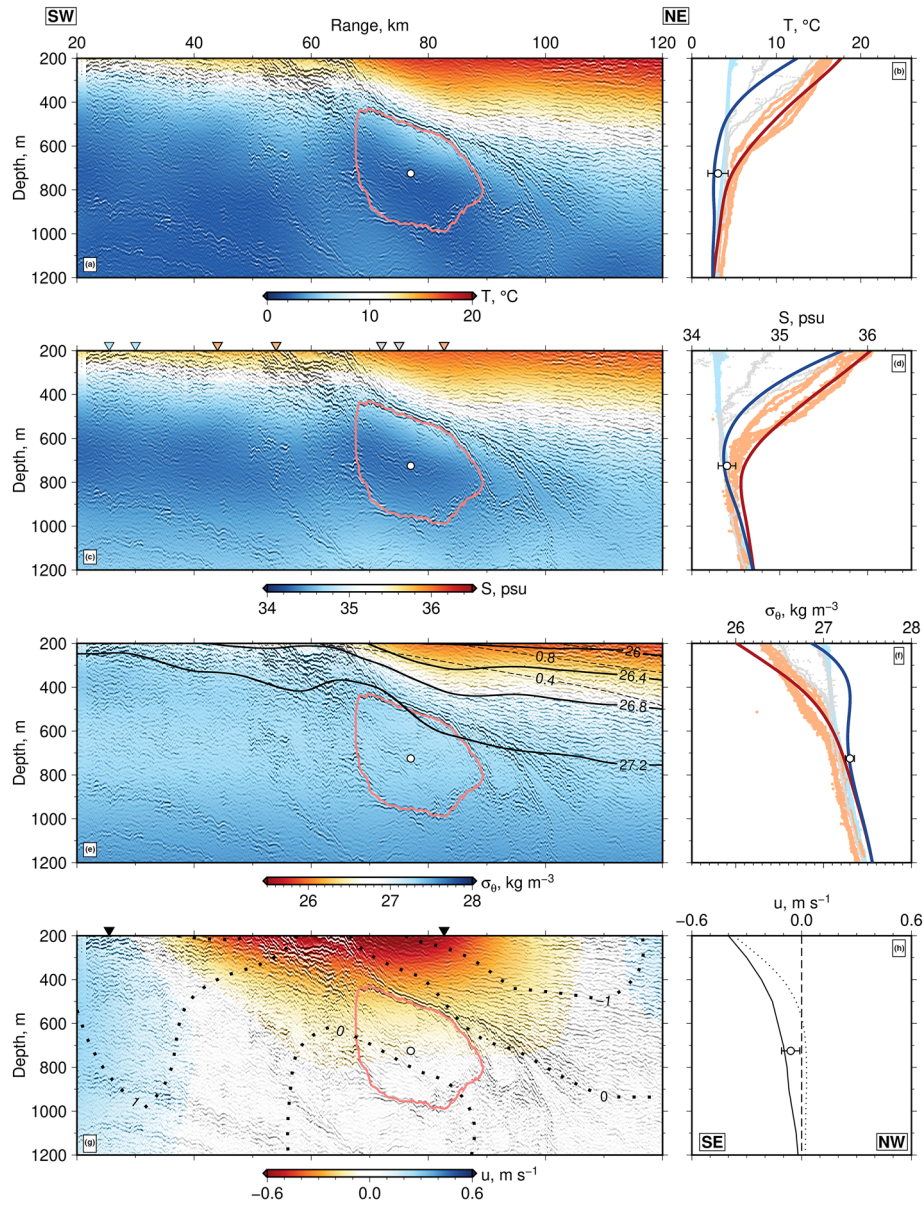


Figure 8. (a) Seismic section overlain with temperature field calculated using iterative inversion procedure (Gunn et al., 2018). Pink area = large lens; white circle = geometric center of large lens. (b) Temperature, T , as a function of depth. Blue/red lines = horizontally averaged profiles for ranges of 0–60 and 60–140 km, respectively; turquoise/orange dots = hydrographic measurements from cold/warm (i.e., MC/BC) sides of front (Figure 5); gray dots = hydrographic measurements from intermediate zone (i.e., modified MC; Figure 5); white circle with horizontal error bar = mean temperature of lens outlined in pink on panel a and its standard deviation. (c) Same section overlain with salinity field. Colored inverted triangles = orthogonally projected positions of seven hydrographic casts where turquoise symbols = Malvinas Current, orange symbols = Brazil Current, and gray symbols = intermediate water (Figure 1a Piola & Matano, 2017). (d) Salinity, S , as a function of depth with colored lines and symbols as before. (e) Same section overlain with potential density field. Solid lines = contours of isopycnal surfaces with values of σ_θ plotted at 0.2 kg m^{-3} intervals; dashed lines = contours of geostrophic stream function, ψ , plotted at $0.2 \times 10^4 \text{ m}^2 \text{ s}^{-2}$ intervals. (f) Potential density, σ_θ , as a function of depth with colored lines and symbols as before. (g) Same section overlain with geostrophic velocity field where warm (cool) colors denote translation out of (into) page. Dotted lines = contours of relative vorticity, ζ , plotted at $5 \times 10^{-5} \text{ s}^{-1}$ intervals; black inverted triangles = loci used to calculate profile of u on panel h. (h) Geostrophic velocity, u , as a function of depth. Solid line = profile of u calculated for two nearby hydrographic profiles projected orthogonally by 8 and 16 km onto seismic section at ranges of 25.5 and 82.7 km (Figure 1a); dotted line = profile of u calculated between black circles located at ranges of 25.5 and 82.7 km on section from panel g; white circle with horizontal error bar = mean geostrophic velocity of eddy and its standard deviation; dashed vertical line = zero value.

Table 2
Near-Coeval Hydrographic Casts Whose Locations Are Shown in Figures 1a, 2, and 5

Name	dd/mm/yyyy	Latitude (°S)	Longitude (°W)
T1	15/11/2012	53.36	36.86
T2	28/11/2012	53.08	36.43
T3	04/12/2012	53.40	36.72
T4	12/12/2012	53.02	36.43
T5	20/12/2012	53.32	36.60
T6	29/12/2012	52.97	36.36
T7	09/01/2013	53.04	36.66

4.2. A Large Tilted Lens

Time-lapse imagery shows that the prominent and acoustically blank patch of water shown in Figure 3 appears, grows to a maximum cross-sectional area of $\sim 20 \text{ km}^2$, and disappears over a 9 day period between 8 and 17 February 2013 (Figures S1 and S2; Table 3). The essential aspects of this transient behavior are summarized in Figure 9. On 8 February, no lens is visible adjacent to the front (Figure 9a). On 11 February, a small lens with a cross-sectional area of $\sim 3 \text{ km}^2$ is visible at a range of 100 km and at a depth of 800 m (Figure 9b). This lens continues to grow and reaches a maximum cross-sectional area of $\sim 14 \text{ km}^2$ by 14 February (Figure 9d). It rapidly shrinks on subsequent images and it has

almost completely disappeared by 17 February. Assuming that the lens is an oblate spheroid that grows at a constant rate until it has a principal axis of 35 km and a thickness of 700 m, its volume increases by $\sim 150 \text{ km}^3$ each day during the growth phase. Additional images from Transects 5–8, which temporally interleave with Transects 1–4 but are spatially offset northwestward by $\sim 14 \text{ km}$, corroborate the cycle of growth and decay (Figure 9e and supporting information). During this cycle, the lens migrates southwestward with the advecting front (Figure 9f). We note in passing that additional transects acquired between 22 and 28 April show a second large lens that grows and decays on a similar time scale.

It is straightforward to discount two alternative explanations for these time-lapse observations. First, an unchanging lens could have translated across the survey in a direction that is parallel to the southeastward flowing frontal jet. In this case, areal change will arise because an identical lens is intersected at different times by different transects. Figure 8g shows that calculated geostrophic current perpendicular to the front is consistent with a southeastward jet of up to 0.8 m s^{-1} that is focused on the less dense side of the front and decreases with depth. If the lens is embedded within this geostrophic flow, it will advect at $\sim 0.1 \text{ m s}^{-1}$ and translate by $>60 \text{ km}$ in a 7 day period. If the lens has a diameter of $\sim 20 \text{ km}$, it will translate across the survey box within ~ 2 days, which demonstrates that this explanation is implausible. Second, two separate lenses that migrate southwestward with the advecting front can be invoked. These lenses have diameters that are less than 14 km across (i.e., the orthogonal distance between Transects 1–4 and 5–8). If each lens is assumed to be an oblate spheroid where any one transect represents a slice parallel to the semimajor axis, the required geometric planforms are fluid dynamically implausible. We conclude that the scheme presented in Figure 10b represents a parsimonious history of growth and decay that honors observations from all eight transects. For simplicity, we have assumed that the center of the lens lies between Transects 1–4 and 5–8 but it is important to emphasize that more complicated trajectories yield similar cycles of growth and decay.

4.3. Mesoscale and Submesoscale Features

There is a striking and consistent contrast between patterns of reflectivity that develop on each side of the front (Figure 3). On all eight transects, BC water is characterized by a triangular wedge of flat reflections that sometimes form discrete and continuous bands (supporting information). In contrast, the reflectivity of MC

Table 3
Position and Dimensions of Large lens

Label	Range (km)	Depth (m)	Length (km)	Thickness (m)	Area (km^2)
1	—	—	—	—	—
2	92–105	600–950	11	250	2.2
3	72–88	550–890	16	290	3.6
4	41–69	500–1,200	27	650	13.8
5	67–88	450–1,000	22	400	6.9
6	44–75	450–1,400	34	750	20.0
7	26–47	600–1,100	20	450	4.6
8	—	—	—	—	—

Note. Quoted ranges and depths refer to length of lens projected to surface and its thickness (see Figures S1 and S2). Length and thickness are estimated along major and minor axes of lens, which is typically banked against dipping front. Cross-sectional area calculated assuming that lens can be represented by ellipse.

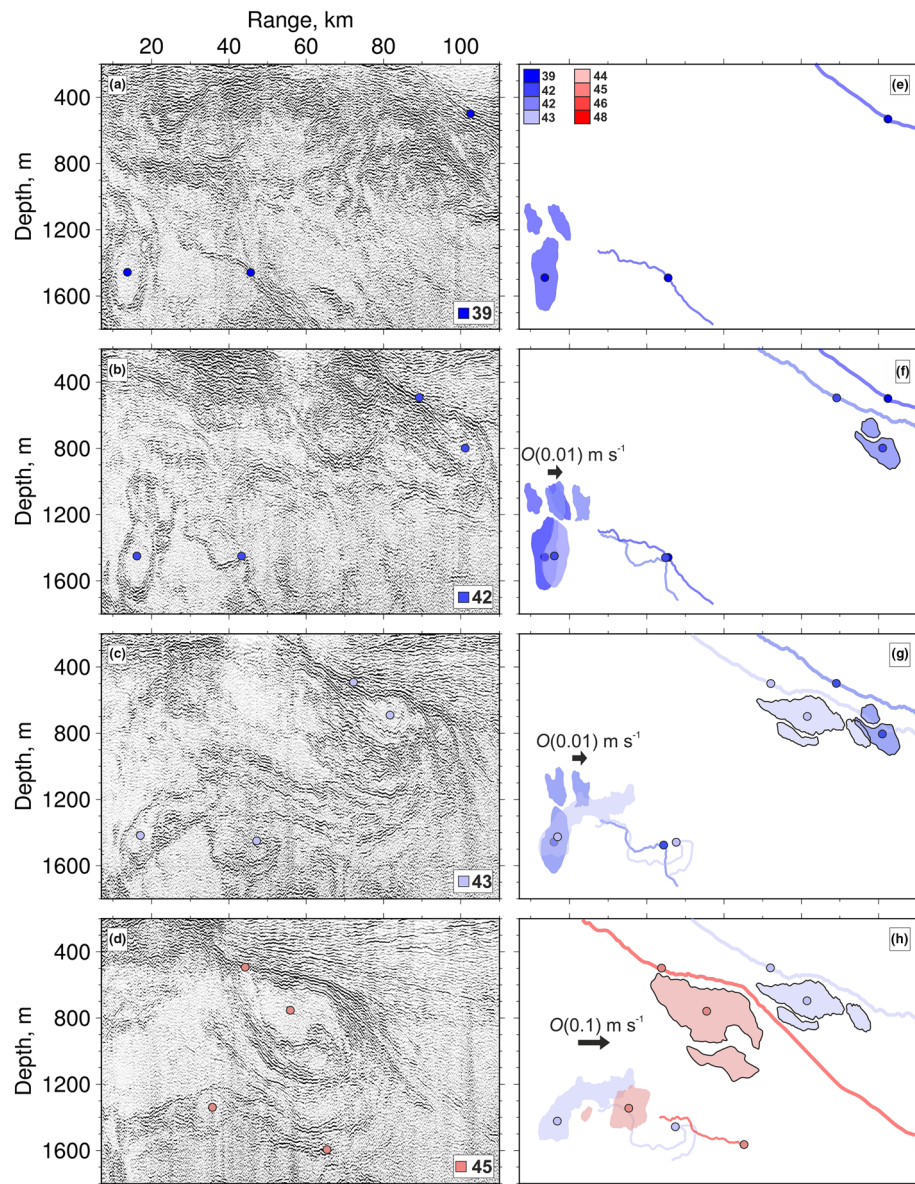


Figure 9. Series of time-lapse images from seismic reflection Sections 1–4 of Figure S1 that show evolving structure adjacent to front. (a) Image from Section 1 (8 February 2013, Julian Day 39). Circles = interpretation markers colored according to day of acquisition that highlight three features; arrows = locus of front; numbered colored square = Julian day (see Table 1 and Figure 2). (b) Image from Section 2 (11 February 2013, Julian Day 42). Symbols as before. (c) Image from Section 3 (12 February 2013, Julian Day 43). (d) Image from Section 4 (14 February 2013, Julian Day 45). (e) Interpretation of Section 1 shown in panel a. Dark blue blobs and lines = interpretation of lenses and strands (note that no clear front is visible in Section 1). Interpretation markers colored according to day of acquisition as shown in key. (f) Combined interpretation of Sections 1 and 2 that highlights temporal evolution of four principal features. Dark/light blue blobs and lines = lenses, strands and fronts at earlier/later times; black arrow = in-plane speed. (g) Same for Sections 2 and 3. (h) Same for Sections 3 and 4.

water has numerous complex swirling features that include lenses and bands. Time-lapse seismic imaging provides a unique opportunity to track the spatial and temporal evolution of these features and to describe their relationship with the migrating front and with the large tilted lens. Here, a preliminary examination of a time-lapse sequence of cross sections taken from Transects 1–4 is carried out (Figure 9).

On Section 1, at a depth of 1,450 m and at a range of 15 km, a circular band of reflectivity is observed. This ~50 m thick band wraps around an acoustically blank core that is ~9 km long and 500 m thick (Figures 9a

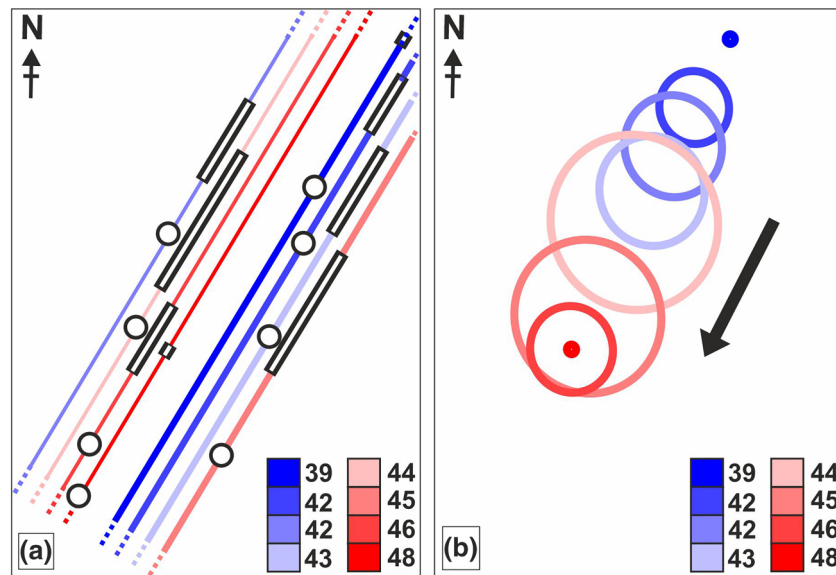


Figure 10. Planform evolution of large tilted lens. (a) Map showing locations of eight sections (Figures S1 and S2). Thick and thin colored lines = Sections 1–4 and Sections 5–8 colored by Julian day of acquisition; white circles = loci of frontal interface projected to sea surface; white bars = horizontal length of putative lens projected to sea surface. (b) Series of planforms of idealized circular lens showing evolution in accordance with geometric constraints from panel e (Table 3). Colored circles = size of lens according to Julian day; arrow = azimuth of translation. Note that panels are vertically collinear.

and 9e). On Section 2, a similar band of reflections occurs at a depth of 1,450 m and at a greater range of 18 km (Figures 9b and 9f). Two days later, this band is seen on Section 3 where it is now tilted and stretched toward the northeast (Figure 9c). On Section 4, the upper portion of this band of reflectivity is now centered at a depth of 1,350 m and at a range of 35 km (Figures 9d and 9h). We interpret this evolving pattern of reflectivity as a single thermohaline structure that is simultaneously deformed and translated toward the northeast (Figures 9g–9i). Northeastward advection of the center of this band is of $O(0.01) \text{ m s}^{-1}$ between 8 and 12 April. This rate increases by an order of magnitude between 12 and 14 April (Figures 9f–9g). These estimates do not consider out-of-plane motion but it is significant that translation of this feature is in the opposite direction to advection of the main front. On the same profiles, elongate continuous reflections, which originally lie at a depth of 1,300–1,800 m and at a range of 25–60 km on Figure 9a, deform and stretch into the filament-like entities visible on Figures 9c and 9d. Note that translation of these different features coincides with growth of the large tilted lens (Figures 9a–9d).

5. Discussion

We present time-lapse imagery from a 3-D seismic reflection survey that straddles the Brazil-Malvinas Confluence. This survey has been calibrated by hydrographic and satellite observations. The availability of time-lapse imagery significantly advances our ability to observe and analyze the structure and evolution of thermohaline fronts whose fluid dynamics are poorly understood. The implications of our results can be divided into two parts. First, the detailed surficial structure of the clearly observed front is examined. Second, the transient behavior of the large tilted lens that sits against the front at depth is considered.

5.1. Near-Surface Frontal Structures

A sharp front that separates BC and MC water masses and intensifies horizontal gradients of temperature and salinity can be continuously traced from the sea surface to depths of 1,500–2,000 m (Figures 1 and 3). Its dramatic continuity through time and space demonstrates that sharp fronts are not necessarily surficial features confined to a thermoclinic layer of several hundred meters thickness. Furthermore, the BC and MC water masses separated by this front have distinctive reflectivity patterns from the sea surface to abyssal depths.

Within 500 m of the sea surface, this major front splits into a series of discrete bright reflective strands that define small tilted lenses with acoustically blank interiors. Time-lapse imagery reveal that these lenses have diameters of ~ 10 km and thicknesses of 200–400 m. Their perimeters are characterized by large-amplitude internal waves. They are probably intrathermocline eddies since they closely resemble homogeneous tongues of weak stratification that occur between pairs of sloping isopycnal surfaces within the thermocline (Pollard & Regier, 1992). Voorhis and Bruce (1982) and Pollard and Regier (1992) carried out high-resolution hydrographic surveys which were used to describe shallow-intensified eddies that strain the surface temperature field into elongated tongues of alternately cold and warm water. Such frontogenic features can be generated by eddy surface shear or by extracting potential energy from the mixed layer (Pollard & Regier, 1992). They are affected by air-sea interactions on time scales of weeks.

Spall (1995) describes a frontogenetic model whereby naturally induced vertical variation of the along-front velocity generates shear instabilities (Figure 8g). If stratification is weak, parcels of low potential vorticity (i.e., homogeneous boli of mixed water) tend to subduct beneath the front. Analytical and numerical models that include these mechanisms produce anticyclonic eddies at depths of ≤ 100 m with dimensions that are consistent with observed radii (i.e., $L_R \approx 1$ km). These eddies are long lived and can transport anomalous water properties thousands of kilometers away from their site of formation (D'Asaro, 1988; Spall, 1995; Thomas & Ferrari, 2008). In contrast, Thomas and Shakespeare (2015) develop an analytical model which shows that frontogenesis and cabbeling can cause mode water formation at confluent fronts, provided that the front is density compensated. Subsurface anticyclones with dimensions of $O(10)$ km are generated at the depth of maximum cross-front temperature. Cross-front temperature gradients are greatest close to the surface (Figure 4).

We conclude that the small tilted lenses imaged on all eight transects are generated by near-surface frontogenetic processes. Surface-trapped eddies can play a significant role in the transport of properties between the thermocline and the mixed layer. Voorhis and Bruce (1982) reported vertical and cross-front velocities of $30\text{--}50\text{ m day}^{-1}$ and $3\text{--}5\text{ km day}^{-1}$, respectively. Their presence throughout the seismic volume suggests that they are ubiquitous in the vicinity of the Brazil-Malvinas Confluence and play a key role in water mass modification close to the surface.

5.2. A Deep Transient Lens

We observe a large tilted lens that is embedded within the front which it appears to deform. This lens grows and decays over a 9 day period. Its size, depth and transience are inconsistent either with the characteristics of a typical intrathermocline eddy or with typical near-surface frontogenetic processes. By combining our time-lapse seismic observations with near-coeval hydrographic measurements and with fluid dynamical considerations, limited inferences can be made which shed some light on the possible mechanism of formation of this unusual transient structure.

5.2.1. Mechanisms of Growth

The lens consists of cool ($3.3 \pm 1^\circ\text{C}$) and fresh (34.3 ± 0.5 psu) water, which implies that it is sourced from the southwestern side of the front (i.e., from modified MC water; Figures 8b and 8d). Although the lens attains mesoscale dimensions, we regard it as nongeostrophic (i.e., ageostrophic). On the cold fresh side of the front, numerous irregular and elongate reflective features can be traced from the southernmost edge of each transect toward the base of the large lens (Figure 3b). Time-lapse imagery demonstrates that these features are being rapidly and horizontally advected toward the front (Figures 9a–9d). They have similar dimensions to axisymmetric filaments that have widths of < 10 km and lengths of hundreds of kilometers (Lapeyre & Klein, 2006; McWilliams, 1984; Rudnick & Ferrari, 1999; Smith & Ferrari, 2009). Such filaments are characterized by weak density signatures and so can be generated by isopycnal stirring induced by rotation of an eddy (Smith & Ferrari, 2009). Observed straining and shearing of reflective filaments may provide the advective mechanism by which cold fresh water is drawn into the large deep lens (Figure 9).

Horizontal translation is probably accompanied by a component of vertical flux that could be facilitated by ageostrophic circulation, by isopycnal tilting, or by injection of energy. At the Brazil-Malvinas Confluence, isopycnal surfaces beneath 700 m have slopes that are close to 0, which suggests that vertical motions overcome the effects of density through ageostrophic circulation or energy injection. Ageostrophic circulation generates significant, $O(10)\text{ m day}^{-1}$, vertical velocities that are induced at a front to restore geostrophic balance (Hoskins & Bretherton, 1972). For the distribution of potential density and geostrophic vorticity shown

in Figure 8, ageostrophic velocities are generated that transport cold water to the northeast (see Figure 12 of Pollard & Regier, 1992). A closed cell of effectively horizontal vorticity is induced such that deep water is uplifted at the northeastern edge of the circulation cell (Hoskins & Bretherton, 1972).

Propagating, near-inertial waves can also be trapped against, amplified by, and aligned with tilted isopycnal surfaces (Whitt & Thomas, 2013). These waves can be generated by wind events, which can inject significant energy at depth. They also interact with frontal density gradients in the presence of strong baroclinic shear, following some form of energy injection (e.g., wind forcing, instabilities; Kunze, 1986; Thomas, 2017). It is straightforward to test the strength of baroclinicity (Whitt & Thomas, 2013). Strongly baroclinic flows are defined as ones with a gradient Richardson number, $Ri_g = N^2 / |\partial u / \partial z|^2$, of $O(1)$. Given $N \approx 1 \times 10^{-3} \text{ s}^{-1}$ and $|\partial u / \partial z| \approx 1 \times 10^{-4} \text{ s}^{-1}$ (i.e., $0.6 \text{ m s}^{-1} / 1,200 \text{ m}$), we obtain $Ri_g = 100$ which implies that the front is weakly sheared (Figure 6h). Analysis of mean wind stress during February 2013 confirms that no significant energy injection took place during acquisition of the seismic survey (Figure 4i). Although teleconnections may exist between sea surface temperature of the South Atlantic Ocean and the El Niño phenomenon through the Antarctic Circumpolar Wave such that that distal energy injection is a possibility, the combination of a high value of Ri_g and the lack of an obvious energy injection mechanism suggests that near-inertial waves did not generate the large tilted lens. Nevertheless, we suspect that interaction of internal gravity waves along frontal density gradients is a possible candidate for generating the features that we observe. For example, Shakespeare and Taylor (2014) report that inertia gravity waves can be spontaneously generated at confluent fronts since time-varying strain produces finite amplitude waves that are strongly localized in time and space.

Finally, vertical shear generated by the frontal jet injects kinetic energy which can be converted into potential energy. The kinetic energy density is given by $\rho(\Delta u)^2/2$, where Δu is the difference in current speed across the front. The potential energy density required to lift a parcel of water through a vertical distance, Δh , is given by $\Delta \rho g \Delta h$, where ρ and g are potential density and gravitational acceleration, respectively. The maximum value of Δh is given by

$$\Delta h \approx \frac{(\Delta u)^2}{2g'} \quad (2)$$

where $g' = g\Delta\rho/\rho$. The value of Δh can be gauged from distribution of ρ and u calculated from seismic images (Figure 8). At a depth of 750 m, $\Delta\rho$ is $O(0.01) \text{ kg m}^{-3}$ and $(\Delta u)^2$ is $O(0.1) \text{ m}^2 \text{ s}^{-2}$, yielding $\Delta h \sim O(170 \text{ m})$. At a depth of 300 m, $\Delta\rho$ is $O(0.1) \text{ kg m}^{-3}$ and $(\Delta u)^2$ is $O(0.01) \text{ m}^2 \text{ s}^{-2}$, yielding $\Delta h \approx 0 \text{ m}$.

These estimates suggest that vertical fluxes of $O(100) \text{ m}$ can exist at depths of 750 m, which are consistent with vertical separation between the core of the large tilted lens at 750 m and elongated filaments at $>1,000 \text{ m}$. We conclude that these filaments provide the mechanism by which cold water feeds the lens. It is unlikely that the lens forms by subduction of surface water or by injection of energy close to the surface, although spontaneous generation of internal gravity waves by frontogenesis could trigger this instability. Instead, we suggest that our time-lapse imagery has captured ageostrophic circulation. These arguments imply that there is a coupling between horizontal translation and vertical mixing. Our observations and fluid dynamical inferences are consistent with numerical experiments that predict lateral stirring of temperature and salinity by eddies, which is accompanied by vertical advection through ageostrophic velocity (e.g., Smith & Ferrari, 2009).

5.2.2. Mechanisms of Decay

The large tilted lens decays rapidly over $O(3)$ days. This estimate can be contrasted with the time taken for frictional spin-down, τ , which is given by

$$\tau = \frac{h}{\sqrt{2K|f|}}, \quad (3)$$

where $h \sim 300 \text{ m}$ is the vertical scale of motion, $f \sim 2 \times 10^{-4} \text{ s}^{-1}$ is the Coriolis frequency, and $K = 10^{-4} \text{ m}^2 \text{ s}^{-1}$ is diapycnal diffusivity (Munk, 1966; Pedlosky, 1987). The value of K at oceanic fronts can be as great as $10^{-3} \text{ m}^2 \text{ s}^{-1}$ (D'Asaro et al., 2011). Equation 3 yields $\tau \approx 5\text{--}17$ days. This discrepancy supports our inference that the large tilted lens is not associated with surface processes since frictional spin-down is probably not a viable mechanism.

Hua et al. (2013) show that concentric layering can be an effective mechanism of energy dissipation. Unfortunately, it typically takes ~ 8 months for 20% of the energy to dissipate. We note also that intrathermocline eddies can last for several years despite being adjacent to frictional boundary layers (e.g., Armi et al., 1989). We conclude that the rapid rate of decay of the lens is inconsistent with estimates of frictional spin-down and with simulations of frontogenetically induced eddies. Instead, its short lifespan probably reflects its ageostrophic nature. A combination of translation and decay suggests that it is continuously shedding water on its poleward journey with implications for flux estimates of heat, salt, and nutrients (McWilliams, 1984; Smith & Ferrari, 2009).

6. Conclusions

The scale and complexity of major oceanic fronts presents significant logistic challenges for dynamical interrogation on an appropriate range of spatial and temporal scales. Seismic reflection surveying has a hitherto unsurpassed ability to resolve thermohaline structures on spatial scales of tens of meters to hundreds of kilometers and on temporal scales of minutes to days. In combination with simultaneous hydrographic observations, this ability has the potential to transform our understanding of frontogenesis. Here, we have described a suite of calibrated time-lapse images that enables acoustic reflectivity to be interpreted from a physical oceanographic perspective. Eight seismic transects reveal a deeply penetrating front, intrathermoclinic eddies, and a large deep transient lens that appears to entrain rapidly deforming filaments. The existence, depth, and longevity of this lens are inconsistent with numerical and analytical simulations of near-surface frontogenesis. Evidence for isopycnal stirring on respective horizontal and vertical length scales of > 50 km and $O(100)$ m has significant implications for flux estimates of heat, salt, and nutrients. These dramatic images reveal stirring at 1–100 km scales with a simultaneous resolution of $O(10)$ m. Perhaps our most significant finding is the depth scale at which these processes occur, implying that frontogenic forcing affects the entire water column. In the future, combined hydrographic and seismic reflection surveying should provide new and important insights.

Data Availability Statement

Ocean Surface Current Analysis Real-time (OSCAR), Multi-scale Ultra-high Resolution (MUR) SST Analysis, and Metop-A ASCAT data sets were extracted from ERDDAP (<https://coastwatch.pfeg.noaa.gov/erddap>).

Acknowledgments

K. L. G. was supported by University of Cambridge. The research activity of C. P. C. was supported by EPSRC Programme Grant EP/K034529/1. We are grateful to Administración Nacional de Combustibles, Alcoholes y Portland and to Shell International Exploration and Production for providing seismic field tapes. Access to these tapes and near-coeval hydrographic measurements should be directed to these organizations. Seismic processing was carried out using Omega2 software package provided by Schlumberger Research Services. Hydrographic measurements were analyzed using Python implementation of GSW TEOS-10 equation of state for seawater (github.com/TEOS-10/GSW-Python). Figures were prepared using Generic Mapping Tools (gmt.soest.hawaii.edu). We are grateful to A. Dickinson, D. Bright, I. Frame, C. Jones, D. Lyness, J. Salvage, K. Sheen, S. Stephenson, and A. Woods for their help. Cambridge Earth Sciences contribution number esc.4755.

References

- Armi, L., Hebert, D., Oakey, N., Price, J. F., Richardson, P. L., Rossby, H. T., & Ruddick, B. (1989). Two years in the life of a Mediterranean salt lens. *Journal of Physical Oceanography*, 19(3), 354–370. [https://doi.org/10.1175/1520-0485\(1989\)019](https://doi.org/10.1175/1520-0485(1989)019)
- Bianchi, A. A., Giulivi, C. F., & Piola, A. R. (1993). Mixing in the Brazil-Malvinas confluence. *Deep-Sea Research Part I*, 40(7), 1345–1358. [https://doi.org/10.1016/0967-0637\(93\)90115-J](https://doi.org/10.1016/0967-0637(93)90115-J)
- Cromwell, T., & Reid, J. L. (1956). A study of oceanic fronts. *Tellus*, 8(1), 94–101. <https://doi.org/10.3402/tellusa.v8i1.8947>
- D'Asaro, E. (1988). Generation of submesoscale vortices: A new mechanism. *Journal of Geophysical Research*, 93(C6), 6685. <https://doi.org/10.1029/JC093iC06p06685>
- D'Asaro, E., Lee, C., Rainville, L., Harcourt, R., & Thomas, L. (2011). Enhanced turbulence and energy dissipation at ocean fronts. *Science*, 318, 318–322. <https://doi.org/10.1126/science.1201515>
- Dagnino, D., Sallares, V., Biescas, B., & Ranero, C. R. (2016). Fine-scale thermohaline ocean structure retrieved with 2-D prestack full-waveform inversion of multichannel seismic data: Application to the Gulf of Cadiz (SW Iberia). *Journal of Geophysical Research: Oceans*, 121, 5452–5469. <https://doi.org/10.1002/2016JC011844>
- Dix, C. H. (1955). Seismic velocities from surface measurements. *Geophysics*, 20(1), 68–86. <https://doi.org/10.1190/1.1438126>
- Ferrari, R. (2011). A frontal challenge for climate models. *Science*, 332(6027), 316–317. <https://doi.org/10.1126/science.1203632>
- Garzoli, S. L., & Garraffo, Z. (1989). Transports, frontal motions and eddies at the Brazil-Malvinas currents confluence. *Deep Sea Research Part A, Oceanographic Research Papers*, 36(5), 681–703. [https://doi.org/10.1016/0198-0149\(89\)90145-3](https://doi.org/10.1016/0198-0149(89)90145-3)
- Gordon, A. L. (1989). Brazil-Malvinas confluence—1984. *Deep-Sea Research*, 36(3), 359–384.
- Gunn, K. L., White, N. J., Larter, R. D., & Caulfield, C. P. (2018). Calibrated seismic imaging of eddy-dominated warm-water transport across the Bellingshausen Sea, Southern Ocean. *Journal of Geophysical Research: Oceans*, 123, 3072–3099. <https://doi.org/10.1029/2018JC013833>
- Holbrook, W. S., Páramo, P., Pearce, S., & Schmitt, R. W. (2003). Thermohaline fine structure in an oceanographic front from seismic reflection profiling. *Science*, 301(5634), 821–824. <https://doi.org/10.1126/science.1085116>
- Hoskins, B. J., & Bretherton, F. P. (1972). Atmospheric frontogenesis models: Mathematical formulation and solution. *Journal of the Atmospheric Sciences*, 29(1), 11–37. [https://doi.org/10.1175/1520-0469\(1972\)029<0011:AFMMFA>2.0.CO;2](https://doi.org/10.1175/1520-0469(1972)029<0011:AFMMFA>2.0.CO;2)
- Hua, B. L., Ménesguen, C., Le Gentil, S., Schopp, R., Marsset, B., & Aiki, H. (2013). Layering and turbulence surrounding an anticyclonic oceanic vortex: In situ observations and quasi-geostrophic numerical simulations. *Journal of Fluid Mechanics*, 731, 418–442. <https://doi.org/10.1017/jfm.2013.369>

- Johnston, T. M., Rudnick, D. L., & Pallàs-Sanz, E. (2011). Elevated mixing at a front. *Journal of Geophysical Research*, 116, C11033. <https://doi.org/10.1029/2011JC007192>
- Kunze, E. (1986). The mean and near-inertial velocity fields in a warm-core ring. *Journal of Physical Oceanography*, 16, 1444–1461. [https://doi.org/10.1175/1520-0485\(1986\)016<1444:tmaniv>2.0.co;2](https://doi.org/10.1175/1520-0485(1986)016<1444:tmaniv>2.0.co;2)
- Lapeyre, G., & Klein, P. (2006). Impact of the small-scale elongated filaments on the oceanic vertical pump. *Journal of Marine Research*, 64(6), 835–851. <https://doi.org/10.1357/002224006779698369>
- McWilliams, J. C. (1984). The emergence of isolated coherent vortices in turbulent flow. *Journal of Fluid Mechanics*, 146, 21–43. <https://doi.org/10.1017/S00222112084001750>
- Meunier, T., Ménesguen, C., Schopp, R., & Le Gentil, S. (2015). Tracer stirring around a meddy: The formation of layering. *Journal of Physical Oceanography*, 45, 407–423. <https://doi.org/10.1175/JPO-D-14-0061.1>
- Munk, W. H. (1966). Abyssal recipes. *Deep-Sea Research*, 13(4), 707–730.
- Nagai, T., Tandon, A., Yamazaki, H., Doubell, M. J., & Gallager, S. (2012). Direct observations of microscale turbulence and thermohaline structure in the Kuroshio Front. *Journal of Geophysical Research*, 117, C08013. <https://doi.org/10.1029/2011JC007228>
- Pallàs-Sanz, E., Johnston, T. M., & Rudnick, D. L. (2010). Frontal dynamics in a California Current System shallow front: 1. Frontal processes and tracer structure. *Journal of Geophysical Research*, 115, C12067. <https://doi.org/10.1029/2009JC006032>
- Papenberg, C., Klaeschen, D., Krahmann, G., & Hobbs, R. W. (2010). Ocean temperature and salinity inverted from combined hydrographic and seismic data. *Geophysical Research Letters*, 37, L04601. <https://doi.org/10.1029/2009GL042115>
- Pedlosky, J. (1987). *Geophysical fluid dynamics* (2nd). New York: Springer. <https://doi.org/10.1007/978-1-4612-4650-3>
- Peterson, R. G., & Stramma, L. (1991). Upper-level circulation in the South Atlantic Ocean. *Progress in Oceanography*, 26(1), 1–73.
- Pezzi, L. P., Souza, R. B., Dourado, M. S., Garcia, C. A. E., Mata, M. M., & Silva-Dias, M. A. F. (2005). Ocean-atmosphere in situ observations at the Brazil-Malvinas Confluence region. *Geophysical Research Letters*, 32, L22603. <https://doi.org/10.1029/2005GL023866>
- Piola, A. R., & Matano, R. P. (2017). Ocean currents: Atlantic Western Boundary-Brazil Current/Falkland (Malvinas) Current. Elsevier. <https://doi.org/10.1016/B978-0-12-409548-9.10541-X>
- Pollard, R. T., & Regier, L. A. (1992). Vorticity and vertical circulation at an ocean front. *Journal of Physical Oceanography*, 22, 609–625. [https://doi.org/10.1175/1520-0485\(1992\)022<0609:vavcaa>2.0.co;2](https://doi.org/10.1175/1520-0485(1992)022<0609:vavcaa>2.0.co;2)
- Ruddick, B., Song, H., Dong, C., & Pinheiro, L. (2009). Water column seismic images as maps of temperature gradient. *Oceanography*, 22(1), 192–205. <https://doi.org/10.5670/oceanog.2009.19>
- Rudnick, D. L., & Ferrari, R. (1999). Compensation of horizontal temperature and salinity gradients in the ocean mixed layer. *Science*, 283(5401), 526–529. <https://doi.org/10.1126/science.283.5401.526>
- Sallarès, V., Biescas, B., Buffett, G., Carbonell, R., Dañobeitia, J. J., & Pelegrí, J. L. (2009). Relative contribution of temperature and salinity to ocean acoustic reflectivity. *Geophysical Research Letters*, 36, L00D06. <https://doi.org/10.1029/2009GL040187>
- Saraceno, M., Provost, C., Piola, A. R., Bava, J., & Gagliardini, A. (2004). Brazil Malvinas Frontal System as seen from 9 years of advanced very high resolution radiometer data. *Journal of Geophysical Research*, 109, C05027. <https://doi.org/10.1029/2003JC002127>
- Shakespeare, C. J., & Taylor, J. R. (2014). The spontaneous generation of inertia-gravity waves during frontogenesis forced by large strain: Theory. *Journal of Fluid Mechanics*, 757, 817–853. <https://doi.org/10.1017/jfm.2014.514>
- Sheen, K. L., White, N. J., Caulfield, C. P., & Hobbs, R. W. (2012). Seismic imaging of a large horizontal vortex at abyssal depths beneath the Sub-Antarctic Front. *Nature Geoscience*, 5(8), 542–546. <https://doi.org/10.1038/ngeo1502>
- Sheen, K. L., White, N. J., & Hobbs, R. W. (2009). Estimating mixing rates from seismic images of oceanic structure. *Geophysical Research Letters*, 36, L00D04. <https://doi.org/10.1029/2009GL040106>
- Smith, K. S., & Ferrari, R. (2009). The production and dissipation of compensated thermohaline variance by mesoscale stirring. *Journal of Physical Oceanography*, 39, 2477–2501. <https://doi.org/10.1175/2009JPO4103.1>
- Spall, M., A. (1995). Frontogenesis, subduction, and cross-front exchange at upper ocean fronts. *Journal of Geophysical Research*, 100(C2), 2543. <https://doi.org/10.1029/94JC02860>
- Taylor, J. R., & Ferrari, R. (2011). Ocean fronts trigger high latitude phytoplankton blooms. *Geophysical Research Letters*, 38, L23601. <https://doi.org/10.1029/2011GL049312>
- Testor, P., DeYoung, B., Rudnick, D. L., Glenn, S., Hayes, D., Lee, C., et al. (2019). OceanGliders: A component of the integrated GOOS. *Frontiers in Marine Science*, 6(422). <https://doi.org/10.3389/fmars.2019.00422>
- Thomas, L. N. (2017). On the modifications of near-inertial waves at fronts: Implications for energy transfer across scales. *Ocean Dynamics*, 67, 1335–1350. <https://doi.org/10.1007/s10236-017-1088-6>
- Thomas, L., & Ferrari, R. (2008). Friction, frontogenesis, and the stratification of the surface mixed layer. *Journal of Physical Oceanography*, 38(11), 2501–2518. <https://doi.org/10.1175/2008JPO3797.1>
- Thomas, L. N., & Shakespeare, C. J. (2015). A new mechanism for mode water formation involving cabbeling and frontogenetic strain at thermohaline fronts. *Journal of Physical Oceanography*, 45, 2444–2456. <https://doi.org/10.1175/JPO-D-15-0007.1>
- Thomas, L. N., Tandon, A., & Mahadevan, A. (2008). Ocean modeling in an eddying regime. In *Geophysical Monograph Series 177* (pp. 17–38). American Geophysical Union. <https://doi.org/10.1029/177GM04>
- Tilstone, G. H., Miller, P. I., Brewin, R. J., & Priede, I. G. (2014). Enhancement of primary production in the North Atlantic outside of the spring bloom, identified by remote sensing of ocean colour and temperature. *Remote Sensing of Environment*, 146, 77–86. <https://doi.org/10.1016/j.rse.2013.04.021>
- Verspeek, J., Stoffelen, A., Portabella, M., Bonekamp, H., Anderson, C., & Saldaña, J. F. (2010). Validation and calibration of ASCAT using CMOD5.n. *IEEE Transactions on Geoscience and Remote Sensing*, 48(1), 386–395. <https://doi.org/10.1109/TGRS.2009.2027896>
- Voorhis, A. D., & Bruce, J. G. (1982). Small-scale surface stirring and frontogenesis in the subtropical convergence of the western North Atlantic. *Journal of Marine Research*, 40, 801–821.
- Whitt, D. B., & Thomas, L. N. (2013). Near-inertial waves in strongly baroclinic currents. *Journal of Physical Oceanography*, 43, 706–725. <https://doi.org/10.1175/JPO-D-12-0132.1>
- Yilmaz, Ö. (2001). *Seismic data analysis: Processing, inversion, and interpretation of seismic data*. Society of Exploration Geophysicists. <https://doi.org/10.1190/1.9781560801580>